crystals

MDPI

Article

Lead-Free Piezoelectric Ceramic Micro-Pressure Thick Films

Kai-Huang Chen [1], Chien-Min Cheng [2,*], Ying-Jie Chen [2] and Mei-Li Chen [3]

1 Department of Electronic Engineering, Center for Environmental Toxin and Emerging-Contaminant Research, Super Micro Mass Research & Technology Center, Cheng Shiu University, Chengcing Rd., Niaosong District, Kaohsiung City 83347, Taiwan
2 Department of Electronic Engineering, Southern Taiwan University of Science and Technology, Tainan 710301, Taiwan
3 Department of Electro-Optical Engineering, Southern Taiwan University of Science and Technology, Tainan 710301, Taiwan
* Correspondence: cmin523@gmail.com

Abstract: In this study, non-stoichiometry lead-free piezoelectric ceramic $Li_{0.058}(K_{0.48}Na_{0.535})_{0.966}(Nb_{0.9}Ta_{0.1})O_3$ (LKNNT) thick films were deposited on Pt/Ti/Si substrates using spin-coating method technology to form a LKNNT/Pt/Ti/Si structure of the micro-pressure thick films. Additionally, the influence on the crystalline properties, surface microstructure images, and mechanical properties, and the piezoelectric properties of the non-stoichiometry lead-free piezoelectric ceramic $Li_{0.058}(K_{0.48}Na_{0.535})_{0.966}(Nb_{0.9}Ta_{0.1})O_3$ (LKNNT) thick films were observed, analyzed, and calculated using X-ray diffraction (XRD), field-emission scanning electron microscopy (FE-SEM), focused ion beam (FIB) microscopy, nano-indention technology, and other instruments. This study was divided into two parts: The first part was the investigation into the fabrication parameters and properties of the bottom layer (Pt) and buffer layer (Ti). The Pt/Ti/Si structures were achieved by the DC sputtering method, and then the rapid thermal annealing (RTA) post-treatment process was used to re-arrange the grains and reduce defects in the lead-free $Li_{0.058}(K_{0.48}Na_{0.535})_{0.966}(Nb_{0.9}Ta_{0.1})O_3$ (LKNNT) thick films. In the second part, lead-free $Li_{0.058}(K_{0.48}Na_{0.535})_{0.966}(Nb_{0.9}Ta_{0.1})O_3$ (LKNNT) powder was prepared by the solid-state reaction method, and then acetic acid ($C_2H_4O_2$) solvent was added to form a slurry for spin-coating technology processing. The fabrication parameters, thick film micro-structure, crystalline properties, nano-indention technology, and the piezoelectric coefficient characteristics of the developed lead-free $Li_{0.058}(K_{0.48}Na_{0.535})_{0.966}(Nb_{0.9}Ta_{0.1})O_3$ (LKNNT)/Pt/Ti/Si structure of the micro-pressure thick film devices a were investigated. According to the experimental results, the optimal fabrication processing parameters of the lead-free $Li_{0.058}(K_{0.48}Na_{0.535})_{0.966}(Nb_{0.9}Ta_{0.1})O_3$ (LKNNT) were an RTA temperature of 500 °C, a Ti buffer-layer thickness of 273.9 nm, a Pt bottom electrode-layer thickness of 376.6 nm, a theoretical density of LKNNT of 4.789 g/cm^3, a lattice constant of 3.968×10^{-8} cm, and a d_{33} value of 150 pm/V. Finally, regarding the mechanical properties of the micro-pressure devices for when a microforce of 3 mN was applied, the thick film revealed a hardness of 60 MPa, a Young's modulus of 13 GPa, and an elasticity interval of 1.25 μm, which are suitable for future applications of micro-pressure devices.

Keywords: lead-free; piezoelectric ceramic; micro-pressure; thick films

Citation: Chen, K.-H.; Cheng, C.-M.; Chen, Y.-J.; Chen, M.-L. Lead-Free Piezoelectric Ceramic Micro-Pressure Thick Films. *Crystals* **2023**, *13*, 201. https://doi.org/10.3390/cryst13020201

Academic Editor: Haibo Zhang

Received: 29 December 2022
Revised: 18 January 2023
Accepted: 20 January 2023
Published: 22 January 2023

Copyright: © 2023 by the authors. Licensee MDPI, Basel, Switzerland. This article is an open access article distributed under the terms and conditions of the Creative Commons Attribution (CC BY) license (https://creativecommons.org/licenses/by/4.0/).

1. Introduction

Micro-pressure sensor devices are the main electrical sensor devices for many consumer electronics [1–4]. Of many different micro-pressure sensors, the piezoresistive material sensor has wide applications in many consumer electronics because of its simple structure and economical and highly efficient performance [5,6]. To discuss and develop the sensitivity properties of micro-pressure sensor devices, various materials and simple sensitive structure devices have been investigated and discussed in recent years. Until now, the complexity of the fabrication process and cost increases, different sensor devices

fabrication processing, sensitive thin films deposition, high-temperature processing, and ion implantation processes were selected and necessary. The changes in the production of piezoceramic sensitive elements to thin film elements were also very important in new sensor (oscillator) methods, such as the detection principles of temperature-compensated oscillators with reactance effects on piezoelectric resonators [7,8].

According previous studies, the graphene, the diamond-like carbon (DLC), and nanocrystalline diamond film were widely discussed and self-supporting for nanoscale thickness films [9,10]. In addition, polysilicon thin film was also developed and investigated for its sensitive and mechanical membrane properties for applications in micro-pressure sensors [11].

Recently, micro-pressure theory for intraocular pressure (IOP) devices and intracranial pressure (ICP) application devices has become a very important research topic for the health care projects. High mortality and poor health were effected by high ICP in traumatic brain injuries and high IOP in many glaucoma cases [9–11]. To the decrease in precision and the long-term monitoring health system lack, the experimental measurements of traditional IOP and ICP of micro-pressure electronic devices were usually for health care.

In addition, microelectromechanical systems (MEMS) have driven the advancement of piezoelectric ceramics for the miniaturization and development of electronic devices. In MEMS device fabrication and manufacturing, the components of piezoelectric sensors have recently changed from the original ceramic bulk material to piezoelectric thick films and thin films. Piezoelectric ceramic materials are divided into many types of materials, such as the PZT series, BT series, and KNN series [12–20].

Among them, PZT material systems have revealed excellent properties and characteristics and are currently widely used in industrial product generation. The development of lead-free piezoelectric ceramic materials have become an urgent technology in recent years due to rising environmental awareness. In addition, the KNN material series of lead-free piezoelectric ceramic materials have the most potential for the development of micro-pressure devices. Recently, many deposition and fabrication process methods for thick film and thin film materials, such RF magnetron sputtering, pulsed laser deposition, chemical vapor deposition, and liquid phase synthesis, have been developed. In addition, the liquid phase synthesis method was developed using the sol-gel method because of the low-cost vacuum equipment and low temperature required, and because it easily covers a large-area substrate.

According to many previous studies on KNN, the buffer layer and the bottom electrode layer crack and melt [21–27]. Two often discussed and investigated topics in these KNN-related papers were the thickness variation between the buffer layer, the bottom electrode layer, and the complete film structure after the RTA processing treatment. In this study, acetic acid was added to lead-free piezoelectric ceramic powder to form a lead-free piezoelectric ceramic precursor solution next processing step. To form a $Li_{0.058}(K_{0.48}Na_{0.535})_{0.966}(Nb_{0.9}Ta_{0.1})O_3$ (LKNNT)/Pt/Ti/Si thick film structure, the lead-free piezoelectric ceramic powder spin-coated on the Ti buffer layer was fabricated and investigated in this study. In addition, the mechanical and piezoelectric properties of the microstructure and thin crystalline films were analyzed and investigated. The lead-free piezoelectric (LKNNT) thick films were prepared using pressureless sintering method for the spin-coating process and the solid-state sintering reaction method was used. Finally, these methods were discussed and investigated.

2. Experimental Detail

To discuss the electric properties, the thin crystalline films, thin film thickness, microstructure morphology, and the mechanical parameters and piezoelectric properties of the lead-free ceramic thick film, and the complete ($Li_{0.058}(K_{0.48}Na_{0.535})_{0.966}(Nb_{0.9}Ta_{0.1})O_3$ (LKNNT)) piezoelectric ceramic thick film structure for the substrate, buffer layer, bottom electrode layer, and the lead-free piezoelectric thick film were observed and analyzed. The metal–insulator–metal (MIM) structure diagram is shown in Figure 1.

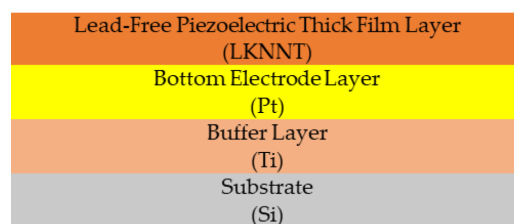

Figure 1. The structure of $Li_{0.058}(K_{0.48}Na_{0.535})_{0.966}(Nb_{0.9}Ta_{0.1})O_3$ (LKNNT) thick film.

The $Li_{0.058}(K_{0.48}Na_{0.535})_{0.966}(Nb_{0.9}Ta_{0.1})O_3$ (LKNNT)/Pt/Ti/silicon metal–insulator–metal (MIM) structure samples shown in Figure 1 were divided to discuss the possible piezoelectric properties of the lead-free piezoelectric micro-pressure devices prepared using spin-coating technology. First, the single Ti buffer thin film layer and the single Pt bottom electrode thin film layer were deposited on the silicon substrate to form Pt/Ti/Si structures. The Pt/Ti metal target of the DC sputtering system was placed 5 cm away from the silicon substrate. To remove the defects of the metal target and obtain stable plasma during the DC sputtering deposition time, the pre-sputtering deposition was maintained for 30 min under the argon gas environment for the as-deposited Pt/Ti thin film prepared. In addition, the sputtering power for the targets was 160 W. After the spin-coating process at room temperature, the as-deposited LKNNT thin film was improved and treated using the rapid temperature annealing (RTA) process. For the RTA processing, the as-deposited LKNNT thin films were annealed and treated at 500 °C for 30 s. To complete the MIM structure, several arrays of the circular top electrode with a diameter of 50 m^2 were formed by Pt top-electrode of 200 nm for DC sputtering technology in the vacuum system operating of 5×10^{-5} Torr.

Then, the thin film thickness variation effects of the 10 min RTA treatments at temperatures of 300, 500, and 700 °C were also investigated in the next treatment process. To prepare the as-deposited lead-free piezoelectric LKNNT thin films, LKNNT powder was prepared using the solid-state reaction method, adding acetic acid ($C_2H_4O_2$) solvents to form a precursor slurry for the spin-coating deposition process. In addition, the as-deposited lead-free piezoelectric thick films were prepared using spin-coating technology on the fabricated Pt/Ti/Si structure, forming the LKNNT/Pt/Ti/Si MIM structure for micro-pressure devices.

To further investigate and determine the thermal annealing treatment effect on lead-free piezoelectric thick films, the electrical and physical properties were investigated and analyzed using scanning electron microscopy (SEM) and X-ray diffraction (XRD) measurements. XRD crystalline analysis, nano-indention analysis, and PFM piezoelectric characteristic analysis of the thick film devices were also carried out and discussed. In addition, the electrical properties of the micro-pressure devices were obtained by an Agilent B1500 semiconductor parameter analyzer. There were about 10 samples per mix for testing. The standard deviations of the d_{33} and deformation amplitude values of the data were presented using cubic notation. In addition, the nano-indention technology was measured by the Hit 300 instrument (maximum load of 500 mN, load noise background of 1 µN, load resolution of 0.02 µN, depth range of 200 µm, displacement resolution of 0.01 nm, and deep noise background of 0.3 nm). In addition, the d_{33} value of the piezoelectric force microscope (PFM) measurement was determined by the IM-8000 (Keyence corporation of America, Itasca, USA) instrument.

3. Results and Discussion

In this study, the experimental details are divided two cases: (1) the thicknesses of thick film of the buffer layer and the bottom electrode layer were determined treated by rapid temperature post-treatment processing, and (2) the electrical and piezoelectric characteristics of the lead-free piezoelectric thick film layer for the non-RTA and RTA-treated samples were compared.

There were differences in the buffer layer and bottom layer of the lead-free piezoelectric thick film for the non-RTA and RTA-treated processing. As shown in Table 1, in forming the Ti/Si structures, the Ti buffer layer was deposited on the silicon substrate prepared by the DC sputtering method for a 1–2 h sputtering time for thicknesses of 50.4 and 205.4 nm, respectively. When the sputtering time was 1 h, the thickness of the Ti (59.92 nm) after the RTA treatment at 300 °C was +19% thicker than that the original thickness (50.4 nm) of the as-deposited thin films. For the sputtering time of 2 h, the thickness of the Ti (162.6 nm) after the RTA treatment at 300 °C was −21% thinner than that of the original thickness (205.4 nm). With the sputtering times of 1 and 2 h, when the RTA temperature increased to 700 °C, the thicknesses of the Ti buffer layer gradually increased to 42.8 (1 h) and 179.8 (2 h) nm, respectively. In addition, the the as-deposited thick thicknesses were −15% (1 h) and −17% (2 h), respectively. This was caused by the uneven release of internal stress of the lead-free piezoelectric thick films during the RTA treatment process, which induced the uneven shrinkage style.

Table 1. The thickness variation of the Ti/Si structure.

Structure	Sputtering Time (Hour)	RTA Temp. (°C)	Film Thickness (nm)	Thickness Ratio (%)
Ti/Si	1	None	50.4	±0
		300	59.92	+19
		500	51.36	+2
		700	42.8	−15
	2	None	205.4	±0
		300	162.6	−21
		500	162.6	−21
		700	179.8	−13

As shown in Table 2, the platinum (Pt) bottom electrode layer was also deposited using the DC sputtering method with the sputtering deposition time of 1 h, forming the Pt/Si structure with a thickness of 470.8 nm. With the RTA post-treatment process at temperatures of 300, 500, and 700 °C, compared to the as-deposited thick thickness (470.8 nm), the thickness of the Pt was gradually reduced from −6 to −22%. According to the above experimental results, the denser and decreases surface microstructure of the lead-free piezoelectric thick films were caused by the thickness internal stress release and re-arrangement of the grains.

Table 2. The thickness variation of the Pt/Si structure.

Structure	Sputtering Time (Hour)	RTA Temp. (°C)	Pt Thickness (nm)	Thickness Ratio (%)
Pt/Si	1	None	470.8	±0
		300	445.1	−6
		500	385.2	−18
		700	368.1	−22

Based on the above experimental results, and using the RF magnetron sputtering again (Pt = 1 h and Ti = 2 h), the Pt (325.3nm)/Ti (256.8 nm)/Si structure was obtained. As shown in Table 3, the thickness of the Pt electrode layer using the RTA treatment at temperatures of 300, 500, and 700 °C increased to 376.6 nm (+16%, 500 °C RTA) and then decreased to 368.1 nm (+13%, 700 °C RTA). For the Ti buffer layer, the thickness first increased to 291 nm (+13%, 300 °C RTA), and then the thick film gradually decreased to 214 nm (−17%, 700 °C RTA). Figure 2 shows the cross-section images and top-view morphology of the Pt/Ti/Si structure of the 500 °C RTA post-treatment process. The thicknesses of the Ti (273.9 nm) and Pt (376.6 nm) layers are also presented.

Table 3. The thickness variation of the Pt/Ti/Si structure.

Structure	Sputtering Time (Hour)	RTA Temp. (°C)	Film Thickness (nm)		Thickness Ratio (%)	
			Ti	Pt	Ti	Pt
Pt/Ti/Si	Pt = 1 h Ti = 2 h	None	256.8	325.3	±0	
		300	291.0	325.3	+13	±0
		500	273.9	376.6	+7	+16
		700	214.0	368.1	−17	+13

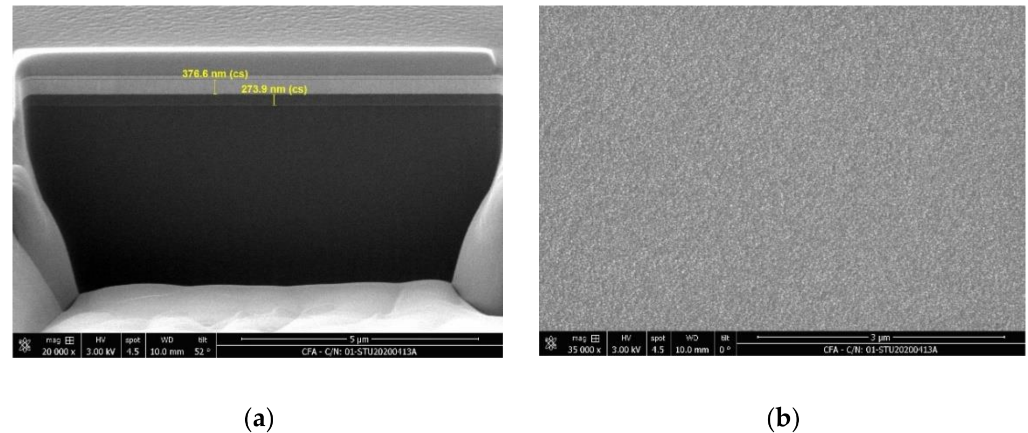

(**a**) (**b**)

Figure 2. The cross-section images and top morphology for (**a**) cross-section view, and (**b**) top view of the Pt/Ti/Si structure.

To compare the electrical and piezoelectric characteristics of the lead-free piezoelectric thick film layer, the $Li_{0.058}(K_{0.48}Na_{0.535})_{0.966}(Nb_{0.9}Ta_{0.1})O_3$ (LKNNT) powder was prepared using the solid-state reaction method at different sintering temperatures of 1050, 1070, 1090, and 1110 °C/4 h, respectively.

Figure 3 presents the surface structure morphology of the XRD measurement details, The strong (100), (001), and (110) preferred peaks and the crystal orientation of the $Li_{0.058}(K_{0.48}Na_{0.535})_{0.966}(Nb_{0.9}Ta_{0.1})O_3$ (LKNNT) thick films gradually increased at the temperature of 1090 °C. At the sintering temperature of 1110 °C, the crystal orientation (100) and (110) preferred peaks were obviously reduced. The crystallinity, lattice constants, and the theoretical densities of the LKNNT thick films are also shown in Table 4. The crystallinity properties and the (110) preferred peaks of the LKNNT did not reach the optimum conditions at the temperature of 1090 °C. The $Li_{0.058}(K_{0.48}Na_{0.535})_{0.966}(Nb_{0.9}Ta_{0.1})O_3$ (LKNNT) powder was prepared at the temperature of 1090 °C, the optimal parameters were chosen, and acetic acid ($C_2H_4O_2$) solvent was added to form a precursor slurry for the spin-coating deposition process based on the above experimental results. The optimal fabricated parameters to buffer layer and bottom electrode layer were used to form the $Li_{0.058}(K_{0.48}Na_{0.535})_{0.966}(Nb_{0.9}Ta_{0.1})O_3$ (LKNNT)/Pt/Ti/Si structure using the spin-coating process method.

Table 4. The XRD patterns of the $Li_{0.058}(K_{0.48}Na_{0.535})_{0.966}(Nb_{0.9}Ta_{0.1})O_3$ (LKNNT) thick film at different sintering temperatures.

Sintering (°C)	1050	1070	1090	1110
$A_{(100)}/A_{total}$	0.730	0.349	0.320	0.317
FWHM (100)	0.198	0.509	0.462	0.525
FWHM (001)	0.184			
$A_{(110)}/A_{total}$	0.270	0.410	0.402	0.407
FWHM (110)	0.301	0.456	0.423	0.506
Lattice constant (10^{-8} cm)	3.942	3.961	3.968	3.959
Theoretical density (g/cm^3)	4.882	4.811	4.789	4.819

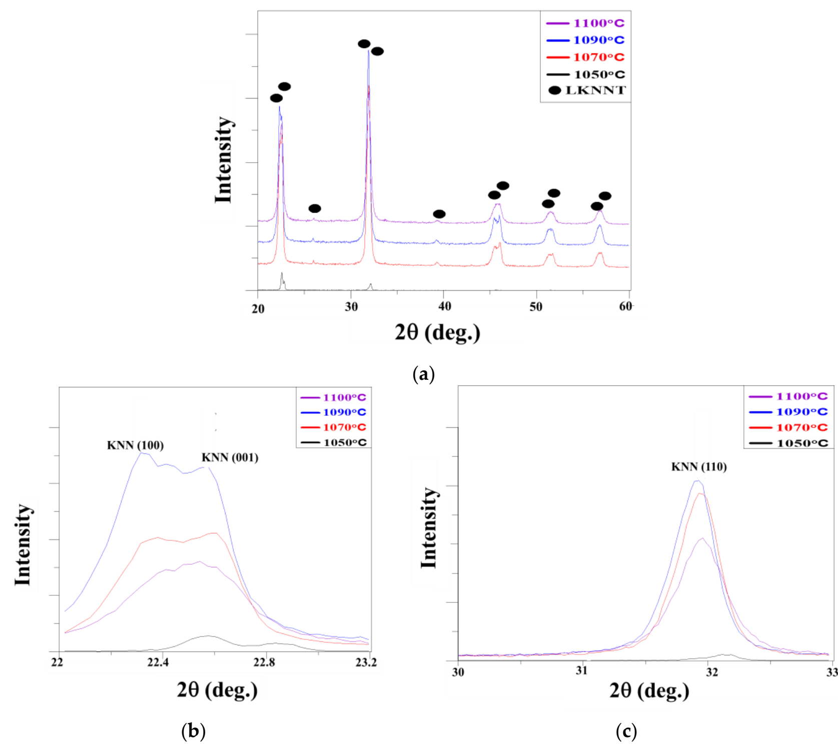

Figure 3. The XRD patterns of the $Li_{0.058}(K_{0.48}Na_{0.535})_{0.966}(Nb_{0.9}Ta_{0.1})O_3$ (LKNNT) thick film under different sintering temperatures for (**a**) 2θ = 20–60°, (**b**) (100) and (001) peaks, and (**c**) (110) peak.

Figure 4 presents the SEM images of the $Li_{0.058}(K_{0.48}Na_{0.535})_{0.966}(Nb_{0.9}Ta_{0.1})O_3$ (LKNNT) thick film under the different RTA temperatures of 300°, 500°, and 700 °C. In addition, the average grain size of the denser and closer LKNNT thick film was about 0.775 µm according to the SEM microscopy image results.

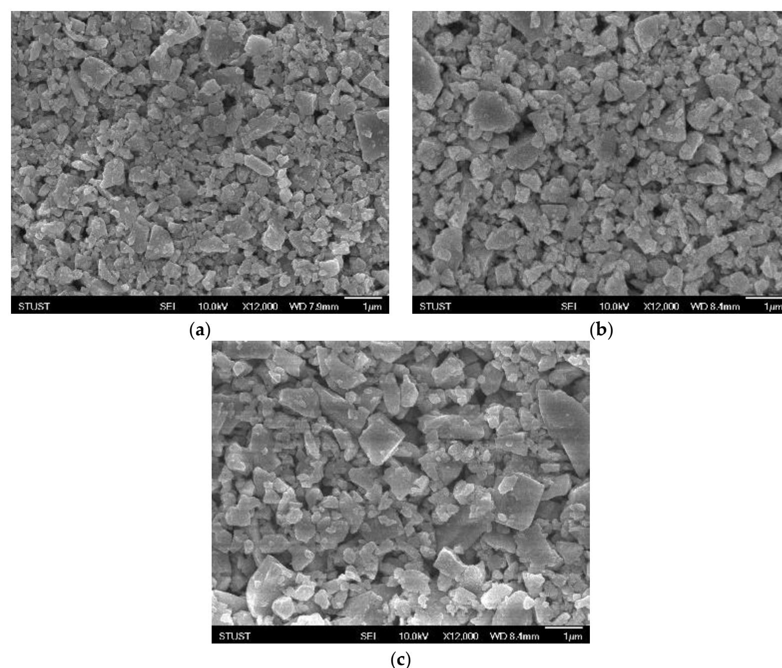

Figure 4. The SEM images of the $Li_{0.058}(K_{0.48}Na_{0.535})_{0.966}(Nb_{0.9}Ta_{0.1})O_3$ (LKNNT) thick film under different RTA temperatures of (**a**) 300°, (**b**) 500°, and (**c**) 700 °C.

Using nano-indention technology, the micro-pressure applied to the lead-free piezoelectric ceramic thick film, and the mechanical properties of the strain, hardness, elastic limit, Young's modulus, and residual stress properties were measured and discussed. Table 5 and Figure 5 present the experimental results of the nano-indention technology. The piezoelectric thick film layer exhibited a low elastic range and harder structure, and a non-regressive displacement curve of the $Li_{0.058}(K_{0.48}Na_{0.535})_{0.966}(Nb_{0.9}Ta_{0.1})O_3$ (LKNNT)/Pt/Ti/Si micro-pressure structure was observed. To the load stress of the micro-pressure devices applied using the nano-indention processing technology, the physical deformation of the $Li_{0.058}(K_{0.48}Na_{0.535})_{0.966}(Nb_{0.9}Ta_{0.1})O_3$ (LKNNT)/Pt/Ti/Si structure occurred and was difficult to restore immediately. Due to the unloading process, the micro-pressure stress was released and the displacement was gradually restored, but the internal residual stress was still not completely released. To release the residual stress of the lead-free piezoelectric of micro-pressure devices was not enough time and difficult to return the original state and shape for the permanent indention. When the hardness of the lead-free piezoelectric thick film increased, low residual stress, high density, and pressure and wear resistance were observed. The cracking effect of the lead-free piezoelectric thick film penetrated and directly pressed the bottom electrode layer and the buffer layer. A cracked gap appeared. On the contrary, the probe distortion and the hardness of the piezoelectric layer decreased were exhibiting high residual stress, low density, and flexible properties. A buffer gap effect was observed for the piezoelectric characteristics of the lead-free piezoelectric thick film.

Table 5. The results of the nano-indention processing of the micro-pressure devices using the lead-free $Li_{0.058}(K_{0.48}Na_{0.535})_{0.966}(Nb_{0.9}Ta_{0.1})O_3$ (LKNNT).

Method	Pressureless Sintering	Solid-State Reaction
Elasticity interval (μm)	2	1.25
Critical stress/deformation (mN/nm)	3.38/2133	3.01/1411
Young's modulus (GPa)	3.629	13.126
Hardness (MPa)	32.528	60.554

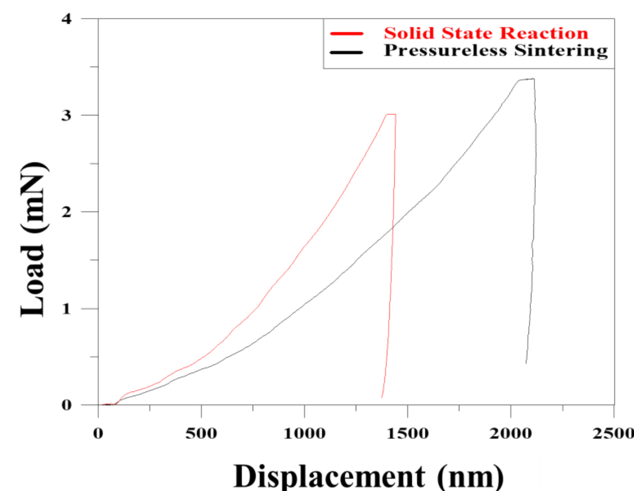

Figure 5. Load–Displacement of the lead-free $Li_{0.058}(K_{0.48}Na_{0.535})_{0.966}(Nb_{0.9}Ta_{0.1})O_3$ (LKNNT) thick film.

The piezoelectric coefficient d_{33} parameters of the $Li_{0.058}(K_{0.48}Na_{0.535})_{0.966}(Nb_{0.9}Ta_{0.1})O_3$ (LKNNT) thick films for micro-pressure devices were obtained and investigated using piezoelectric force microscope (PFM) measurements. the piezoelectric force microscope (PFM) measurement was carried out using DC bias voltage applied between the low electrode of the micro-pressure sample and the probe. The area under the probe became the single polarization region, and the memory unit, area, and strength of the lead-free $Li_{0.058}(K_{0.48}Na_{0.535})_{0.966}(Nb_{0.9}Ta_{0.1})O_3$ (LKNNT) polarization area were also measured. To AC electric field applied to the single

polarization region of the $Li_{0.058}(K_{0.48}Na_{0.535})_{0.966}(Nb_{0.9}Ta_{0.1})O_3$ (LKNNT) samples, and the thick film produced contact-type resonance and induced deformation. The probe lightly pressed on the thick film, and the deformation of the lead-free $Li_{0.058}(K_{0.48}Na_{0.535})_{0.966}(Nb_{0.9}Ta_{0.1})O_3$ (LKNNT) thick film caused by the probe calculated from the circuit and the d_{33} value obtained.

Figures 6 and 7 show the d_{33} values and related output voltages of the lead-free $Li_{0.058}(K_{0.48}Na_{0.535})_{0.966}(Nb_{0.9}Ta_{0.1})O_3$ (LKNNT) thick film of the micro-pressure devices measured and discussed using the PFM experimental results. As shown in fig. 7, the slope proportional to the lead-free piezoelectric coefficient was about 0.0348, and the average d_{33} value was about 150 pm/V in voltage range from 0 to 2 V. Table 6 presents the d_{33} results of the lead-free piezoelectric ceramic thick film. In this study, the d_{33} value of the $Li_{0.058}(K_{0.48}Na_{0.535})_{0.966}(Nb_{0.9}Ta_{0.1})O_3$ (LKNNT) thick film was about 150 pm/V, which is higher than in other reports [28–36].

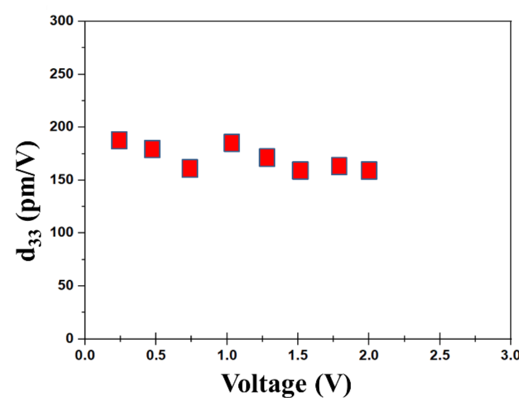

Figure 6. The variation of d_{33} values of the lead-free $Li_{0.058}(K_{0.48}Na_{0.535})_{0.966}(Nb_{0.9}Ta_{0.1})O_3$ (LKNNT) thick films.

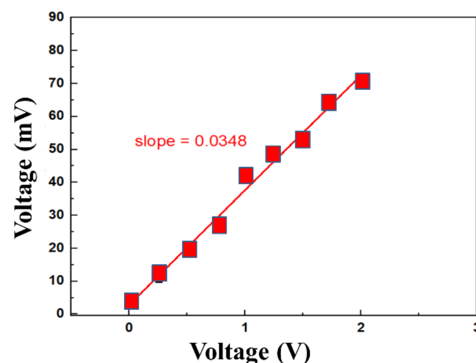

Figure 7. The deformation amplitudes of the lead-free $Li_{0.058}(K_{0.48}Na_{0.535})_{0.966}(Nb_{0.9}Ta_{0.1})O_3$ (LKNNT) micro-pressure devices using the PFM measurement.

Table 6. The d_{33} results of the lead-free $Li_{0.058}(K_{0.48}Na_{0.535})_{0.966}(Nb_{0.9}Ta_{0.1})O_3$ (LKNNT) thin film [28–35].

Material System	Method	d_{33}
KNN	Chemical Solution Deposition	46 pm/V
KNN	Sol-Gel Method	50 pm/V
KNN	RF Magnetron Sputtering	36 pm/V
KNN	Pulsed Laser Deposition	58 pm/V
KNN	Screen Printing Method	138 pm/V
KNN	Chemical Solution Deposition	61 pm/V

4. Conclusions

In conclusion, the effects of the RTA post-treatment for the Ti buffer layer and the Pt bottom electrode layer were analyzed and discussed. Using nano-indention and PFM measurements, the piezoelectric and mechanical properties of the lead-free $Li_{0.058}(K_{0.48}Na_{0.535})_{0.966}(Nb_{0.9}Ta_{0.1})O_3$ (LKNNT) thick film were also determined. In general, the thicknesses of the Ti and Pt layers using RTA post-treatment process became thinner because of the re-arrangement of the crystalline grains of the thick film. The optimal fabrication parameters were an RTA temperature of 500 °C, a thickness of the Ti buffer layer of 273.9 nm, a thickness of the Pt bottom electrode layer of 376.6 nm, a theoretical density of LKNNT of 4.789 g/cm^3, a lattice constant of 3.968×10^{-8} cm, and a d_{33} value of about 150 pm/V. For the mechanical properties of the micro-pressure devices with an applied microforce of 3 mN, the lead-free $Li_{0.058}(K_{0.48}Na_{0.535})_{0.966}(Nb_{0.9}Ta_{0.1})O_3$ (LKNNT) thick film revealed a hardness of 60 MPa, a Young's module of 13 GPa, and an elasticity interval of 1.25 µm.

Author Contributions: K.-H.C. and C.-M.C. designed and performed the experimental work, explained the obtained results, and wrote the paper; K.-H.C. and C.-M.C. conceived the study and participated in its design and coordination; K.-H.C., Y.-J.C., M.-L.C. and C.-M.C. helped in writing of the paper and participated in the experimental work. All authors have read and agreed to the published version of the manuscript.

Funding: This work was performed at the National Science Council Core Facilities Laboratory for Nano-Science and Nano-Technology in the Kaohsiung-Pingtung area and was supported by the National Science Council of the Republic of China under Contract Nos. NSC MOST 110-2637-E-218-008.

Data Availability Statement: Availability Statements are available in section "MDPI Research Data Policies" at https://www.mdpi.com/ethics.

Conflicts of Interest: The founding sponsors had no role in the design of the study; in the collection, analyses, or in-ter-pretation of data; in the writing of the manuscript, and in the decision to publish the results.

References

1. Guan, T.T.; Yang, F.; Wang, W.; Huang, X.; Jiang, B.; Zhang, D.C. The Design and Analysis of Piezoresistive Shuriken-Structured Diaphragm Micro-Pressure Sensors. *J. Microelectromech. Syst.* **2017**, *26*, 206–214. [CrossRef]
2. Lee, D.; Lee, H.; Jeong, Y.; Ahn, Y.; Nam, G.; Lee, Y. Highly Sensitive, Transparent, and Durable Pressure Sensors Based on Sea-Urchin Shaped Metal Nanoparticles. *Adv. Mater.* **2016**, *28*, 9364–9369. [CrossRef] [PubMed]
3. Pandey, V.; Mandal, A.; Sisle, S.; Gururajan, M.; Dusane, R. Piezoresistive pressure sensor using nanocrystalline silicon thin film on flexible substrate. *Sens. Actuators A Phys.* **2020**, *316*, 112372. [CrossRef]
4. Xu, T.; Wang, H.; Xia, Y.; Zhao, Z.; Huang, M.; Wang, J.; Zhao, L.; Zhao, Y.; Jiang, Z. Piezoresistive pressure sensor with high sensitivity for medical application using peninsula-island structure. *Front. Mech. Eng.* **2017**, *12*, 546–553. [CrossRef]
5. Barlian, A.A.; Park, W.; Mallon, J.; Rastegar, A.; Pruitt, B.L. Review: Semiconductor Piezoresistance for Microsystems. *Proc. IEEE* **2009**, *97*, 513–552. [CrossRef] [PubMed]
6. Fiorillo, A.; Critello, C.; Pullano, S. Theory, technology and applications of piezoresistive sensors: A review. *Sens. Actuators A Phys.* **2018**, *281*, 156–175. [CrossRef]
7. Liu, D.; Liu, H.; Liu, J.; Hu, F.; Fan, J.; Wu, W.; Tu, L. Temperature Gradient Method for Alleviating Bonding-Induced Warpage in a High-Precision Capacitive MEMS Accelerometer. *Sensors* **2020**, *20*, 1186. [CrossRef]
8. Matko, V.; Milanovic, M. Temperature-compensated capacitance–frequency converter with high resolution. *Sens. Actuators A Phys.* **2014**, *220*, 262–269. [CrossRef]
9. Smith, A.D.; Niklaus, F.; Paussa, A.; Vaziri, S.; Fischer, A.; Sterner, M. Electromechanical piezoresistive sensing in suspended graphene films. *Nano Lett.* **2013**, *13*, 3237–3242. [CrossRef]
10. Janssens, S.D.; Drijkoningen, S.; Haenen, K. Ultra-thin nanocrystalline diamond films as pressure sensors for harsh environments. *Appl. Phys. Lett.* **2014**, *104*, 073107. [CrossRef]
11. Wang, J.; Chuai, R.; Yang, L.; Dai, Q. A surface micromachined pressure sensor based on polysilicon nanofilm piezoresistors. *Sens. Actuators A Phys.* **2015**, *228*, 75–81. [CrossRef]
12. Gao, F.; Cheng, L.; Hong, R.; Liu, J.; Wang, C.; Tian, C. Crystal Structure and Piezoelectric Properties of $xPb(Mn_{1/3}Nb_{2/3})O_3$—$(0.2\text{-}x)Pb(Zn_{1/3}Nb_{2/3})O_3$—$0.8Pb(Zr_{0.52}Ti_{0.48})O_3$ Ceramics. *Ceram. Int.* **2009**, *35*, 1719–1723. [CrossRef]
13. Yang, Z.; Chao, X.; Zhang, R.; Chang, Y.; Chen, Y. Fabrication and electrical characteristics of piezoelectric PMN–PZN–PZT ceramic transformers. *Mater. Sci. Eng. B* **2007**, *138*, 277–283. [CrossRef]

14. Yang, Z.; Zong, X.; Li, H.; Chang, Y. Structure and Electrical Properties of New $Pb(Zr,Ti)O_3$—$Pb(Fe2/3W_{1/3})O_3$—$Pb(Mn_{1/3}Nb_{2/3})O_3$ Ceramics. *Mater. Lett.* **2005**, *59*, 3476–3480. [CrossRef]
15. Zuo, R.Z.; Fang, X.; Ye, C. Phase Structures And Electrical Properties of new Lead-Free $(Na_{0.5}K_{0.5})NbO_3$—$(Bi_{0.5}Na0.5)TiO_3$ Ceramics. *Appl. Phys. Lett.* **2007**, *90*, 092904. [CrossRef]
16. Wu, J.; Xiao, D.; Wu, W.; Zhu, J.; Wang, J. Effect of Dwell Time During Sintering on Piezoelectric Properties of $(Ba_{0.85}Ca_{0.15})(Ti0.9Zr_{0.1})O_3$ Lead-Free Ceramics. *J. Alloys Comp.* **2011**, *509*, L359–L361. [CrossRef]
17. Su, S.; Zuo, R.; Lu, S.; Xu, Z.; Wang, X.; Li, L. Poling Dependence and Stability of Piezoelectric Properties of $Ba(Zr_{0.2}Ti_{0.8})O_3$—$(Ba_{0.7}Ca_{0.3})TiO_3$ Ceramics with Huge Piezoelectric Coefficients. *Curr. Appl. Phys.* **2011**, *11*, S120–S123. [CrossRef]
18. Lin, D.M.; Kwok, K.; Lam, K.; Chan, H.L.W. Structure and Electrical Properties of $K_{0.5}Na_{0.5}NbO_3$-$LiSbO_3$ Lead-Free Piezoelectric Ceramics. *J. Appl. Phys.* **2007**, *101*, 074111. [CrossRef]
19. Zhang, S.J.; Xia, R.; Shrout, T.; Zang, G.; Wang, J.F. Piezoelectric Properties in Perovskite $0.948(K_{0.5}Na_{0.5})NbO_3$—$0.052LiSbO_3$ Lead-Free Ceramics. *J. Appl. Phys.* **2006**, *100*, 104108. [CrossRef]
20. Guo, Y.; Kakimoto, K.I.; Ohsato, H. Structure and Electrical Properties of Lead-Free $(Na_{0.5}K_{0.5})NbO_3$-$BaTiO_3$ Ceramics. *Jpn. J. Appl. Phy.* **2004**, *43*, 6662–6666. [CrossRef]
21. Zuo, R.; Rödel, J.; Chen, R.; Li, L. Sintering and Electrical Properties of Lead-Free $Na_{0.5}K_{0.5}NbO_3$ Piezoelectric Ceramics. *J. Am. Ceram. Soc.* **2006**, *89*, 2010–2015. [CrossRef]
22. Wang, K.; Zhang, B.-P.; Li, J.-F.; Zhang, L.-M. Lead-free $Na_{0.5}K_{0.5}NbO_3$ piezoelectric ceramics fabricated by spark plasma sintering: Annealing effect on electrical properties. *J. Electroceramics* **2007**, *21*, 251–254. [CrossRef]
23. Kang, J.K.; Lee, Y.; Heo, D.; Lee, H.; Dinh, T.H. Effect of Ta Doping on the Piezoelectric Properties of $(K_{0.5}Na_{0.5})NbO_3$ Ceramics. *J. Korean Inst. Electr. Electron. Mater. Eng.* **2014**, *27*, 292–296.
24. Matsubara, M.; Yamaguchi, T.; Kikuta, K.; Hirano, S.I. Sinterability and Piezoelectric Properties of $(K,Na)NbO_3$ Ceramics with Novel Sintering Aid. *Jpn. J. Appl. Phy.* **2004**, *43*, 7159–7163. [CrossRef]
25. Lim, J.B.; Zhang, S.; Jeon, J.; Shrout, T.R. $(K, Na)NbO_3$-Based Ceramics for Piezoelectric "Hard" Lead-Free Materials. *J. Am. Ceram. Soc.* **2010**, *93*, 1218–1220. [CrossRef]
26. Wu, J.; Wang, Y.; Xiao, D.; Zhu, J.; Yu, P.; Wu, L.; Wu, W. Piezoelectric Properties of $LiSbO_3$-Modified $(K_{0.48}Na_{0.52})NbO_3$ Lead-Free Ceramics. *Jpn. J. Appl. Phy.* **2007**, *46*, 7375. [CrossRef]
27. Zhou, J.J.; Li, J.; Wang, K.; Zhang, X.W. Phase Structure and Electrical Properties of (Li, Ta)-Doped $(K,Na)NbO_3$ Lead-Free Piezoceramics in the Vicinity of Na/K = 50/50. *J. Mater. Sci.* **2011**, *46*, 5111–5116. [CrossRef]
28. Nakashima, Y.; Sakamoto, W.; Maiwa, H.; Shimura, T.; Yogo, T. Lead-Free Piezoelectric $(K, Na)NbO_3$ Thin Films Derived from Metal Alkoxide Precursors. *Jpn. J. Appl. Phy.* **2007**, *46*, L311–L313. [CrossRef]
29. Yu, Q.; Li, J.; Sun, W.; Zhou, Z.; Xu, Y.; Xie, Z.; Lai, F.P. Electrical Properties of $K_{0.5}Na_{0.5}NbO_3$ Thin Films Grown on $Nb:SrTiO_3$ Single-Crystalline Substrates with Different Crystallographic Orientations. *J. Appl. Phys.* **2013**, *113*, 024101. [CrossRef]
30. Li, T.; Wang, G.; Li, K.; Du, G.; Chen, Y.; Zhou, Z.; Rémiens, D.; Dong, X. Electrical properties of lead-free KNN films on SRO/STO by RF magnetron sputtering. *Ceram. Int.* **2013**, *40*, 1195–1198. [CrossRef]
31. Han, G.; Ryu, J.; Ahn, C.-W.; Yoon, W.-H.; Choi, J.-J.; Hahn, B.-D.; Kim, J.-W.; Choi, J.-H.; Park, D.-S. High Piezoelectric Properties of KNN-Based Thick Films with Abnormal Grain Growth. *J. Am. Ceram. Soc.* **2012**, *95*, 1489–1492. [CrossRef]
32. Nguyen, M.D.; Dekkers, M.; Houwman, E.; Vu, H.; Vu, H.; Rijnders, G. Lead-Free $(K_{0.5}Na_{0.5})NbO_3$ Thin Films by Pulsed Laser Deposition Driving MEMS-Based Piezoelectric Cantilevers. *Mater. Lett.* **2016**, *164*, 413–416. [CrossRef]
33. Pavlič, J.; Malič, B.; Rojac, T. Small Reduction of the Piezoelectric d33 Response in Potassium Sodium Niobite Thick Film. *J. Am. Ceram. Soc.* **2014**, *95*, 1497–1503. [CrossRef]
34. Wang, L.; Yao, K.; Ren, W. Piezoelectric $K_{0.5}Na_{0.5}NbO_3$ thick films derived from polyvinylpyrrolidone-modified chemical solution deposition. *Appl. Phys. Lett.* **2008**, *93*, 092903. [CrossRef]
35. Goh, P.C.; Yao, K.; Chen, Z. Lead-free piezoelectric $(K_{0.5}Na_{0.5})NbO_3$ thin films derived from chemical solution modified with stabilizing agents. *Appl. Phys. Lett.* **2010**, *97*, 102901. [CrossRef]
36. Matko, V.; Milanovic, M. Detection Principles of Temperature Compensated Oscillators with Reactance Influence on Piezoelectric Resonator. *Sensors* **2020**, *20*, 802. [CrossRef] [PubMed]

Disclaimer/Publisher's Note: The statements, opinions and data contained in all publications are solely those of the individual author(s) and contributor(s) and not of MDPI and/or the editor(s). MDPI and/or the editor(s) disclaim responsibility for any injury to people or property resulting from any ideas, methods, instructions or products referred to in the content.